Tellus (1995), 47A, 403–420
Printed in Belgium – all rights reserved

TELLUS
ISSN 0280–6495

Interaction of a cold front with a sea-breeze front Numerical simulations

By A. RHODIN*, *Max-Plank-Institut für Meteorologie, Bundesstraße 55, 20146 Hamburg, Germany*

(Manuscript received 11 March 1993; in final form 13 October 1994)

ABSTRACT

This paper presents simulations of a front which passed the coast between the North Sea and northern Germany and thereby experienced some modifications of its mesoscale characteristics. The event was observed during the field experiment FRONTEX'89. The two-dimensional non-hydrostatic simulations presented in this paper resemble some of the observed characteristics and yield a detailed description of the evolution of the surface front. Over the sea several narrow frontal rain bands develop in the boundary layer which becomes unstable due to the increasing sea surface temperature near the coast. The rain bands move forward relative to the the front due to the cross frontal circulation which is enhanced by the release of latent heat in the ascending warm air and by the cooling of the cold air below by evaporating precipitation. Over the heated land surface a sea-breeze front develops ahead of the synoptic-scale cold front. The strong frontal gradients of the sea-breeze front mask the broader frontal zone of the cold front at the ground. The sea-breeze front triggers deep convection ahead of the cold front in the afternoon and takes over all characteristics of the synoptic-scale front in the evening. The simulations show the mechanisms that caused the observed evolution and modification of the synoptic-scale cold front. They emphasize the strong influence of the surface heat fluxes on the characteristics of fronts on the mesoscale. The most important feature of the numerical model, necessary for the proper representation of the frontal characteristics on the mesoscale, is its high resolution. The simulations are restricted by the difficulties of finding an initial state and appropriate boundary conditions so that the results fit the observations for a long time period and that spin-up problems are avoided.

1. Introduction

The evolution of sharp surface fronts from large-scale baroclinic zones is described by the semigeostrophic theory (Hoskins and Bretherton, 1971). The theory predicts the generation of discontinuities at the ground by the frontogenetic cross-front ageostrophic flow caused by the disturbance of the thermal balance by a geostrophic deformation or shear field. Strong surface fronts are observed with a scale of 1 km or less (Shapiro et al., 1985), but there remain a lot of questions regarding the mechanisms responsible for specific mesoscale features.

The generation of strong surface fronts forced by a geostrophic deformation field has been obtained in high-resolution numerical simulations based on the primitive equations. (Gall et al., 1987). This simulations do not show any limitation in the development of the frontal zone to a discontinuity besides the grid size of the numerical model. Yet the simulated frontal patterns are not very similar to observed ones. It was proposed that turbulent mixing should be an important process that limits the cross-front scale of the surface front (Emanuel, 1985). Indeed numerical simulations of fronts driven by a geostrophic shear field with a parameterization of the turbulent fluxes in the boundary layer show more realistic features (Keyser and Anthes, 1982), but these simulations cannot resolve the scale of observed sharp surface fronts of 1 km or less due to the grid size of 40 km. Strong

* Present affiliation: GKSS Research Center, Max Plank Straße, D-21502 Geesthacht, Germany.

surface fronts with realistic mesoscale patterns can be obtained if the grid size is reduced to a scale below 1 km and the dependence of the turbulent momentum transfer on thermal stability is properly taken into account. It was shown that the frictional convergence in the boundary layer is able to reduce the cross-front scale of the surface front from 100 km down to 1 km, without the presence of surface heat fluxes and without a large scale deformation or shear field (Dunst and Rhodin, 1990). These simulations yielded patterns of the sharp surface front similar to a density current head. Thus it turns out, that turbulent friction must not necessarily weaken the surface front but on the contrary may act frontogenetically. In any case it has a distinct impact on its mesoscale appearance.

These theoretical concepts and numerical simulations do not account for diabatic processes as surface heat fluxes, radiation divergences, condensation and evaporation. Therefore they cannot resemble the variety of mesoscale frontal features, which are in particular visible in cloud- and rain bands of different size (see, e.g., the review from Houze and Hobbs, (1982)). Indeed simulations with a horizontal resolution of 5 km and condensation and evaporation processes included produce several kinds of frontal rain bands (Bénard et al., 1992).

This paper focuses on the interaction of the frontal dynamics and boundary layer processes. The mesoscale frontal characteristics depend as well on the large-scale environment and on the local conditions, i.e., the roughness and temperature of the underlying ground and the availability of moisture and latent heat. These conditions may vary to a large extent and therefore it is difficult to draw general conclusions regarding the mesoscale development of fronts. Thus it seems to be more promising to perform case studies in order to investigate the behavior of fronts in certain situations. Especially the frontal passage at a coastline with different surface parameters over sea and land is a good opportunity to investigate the relations between the characteristics of the ground and of the front, respectively.

For this purpose the field experiment FRONTEX'89 (Brümmer, 1990) was performed at the coast of the North Sea. The front observed on 9 May 1989 is the object of this case study. For another frontal event of the campaign (Hennemuth et al., 1992) a distinct influence of the turbulent heat, moisture, and momentum fluxes at the sea surface has already been proven. Crucial dependence of the frontal characteristics on the underlying surface also appears in this case study. The cold front passed the coast of North Germany and whereby experienced a change of its mesoscale characteristics. A detailed description of the observational findings is presented in the accompanying paper of Brümmer et al. (1995). That paper is hereafter referred to as BHRT95. Over the sea the surface front was characterized by a broad baroclinic zone with several narrow cloud bands embedded. The narrow cloud bands were about 20 km wide and 2000 m high and were located ahead of a 200 km wide cloud band at a higher level. Over the land the baroclinic zone contracted to a sharp front that developed from a sea-breeze front and was accompanied by only one compact cloud band of 20 to 30 km width, followed by a 70 km wide cloud gap.

This paper figures out the processes that cause the observed development and modification of the front on the mesoscale by means of high-resolution two-dimensional numerical simulations. A description of the numerical model, the derivation of the initial state from the observations, and the choice of the large-scale deformation field is given in Section 2.

These simulations deal with the development of the mesoscale features of the front before it passed the coast, and the interaction with the sea-breeze front thereafter. It turns out to be impossible to cover all aspects of the observed frontal development in one simulation. Thus the different stages of the frontal evolution are investigated in different runs. In Section 3 the generation of the cloud bands which were observed over the North Sea is discussed and in Section 4 the evolution of the sea-breeze front and its effect on the approaching synoptic scale front is investigated. A summary is given in Section 5.

2. Numerical model and initial state

The prognostic variables of the non-hydrostatic numerical model are potential temperature Θ, cross-front wind u (in the model plane), along-front wind v (perpendicular to the model plane), vertical velocity w, specific humidity q, cloud water content q_c, and rain water content q_r. The turbulent fluxes are parameterized by means of an exchange coefficient derived from the turbulent kinetic energy, which is calculated as a prognostic variable too. A model description is given in the appendix.

The model has several specific characteristics in order to simulate the behavior of fronts. It possesses an non-equidistant grid in horizontal and vertical direction in order to resolve the processes in the vicinity of the surface front on a horizontal scale of a few kilometers and on a vertical scale of some hundred meters in the boundary layer, and to cover the domain of the synoptic-scale front of about 1000 km as well. The model is limited to two dimensions, i.e., to a $x-z$-plane perpendicular to the front. Nevertheless, the influence of the three-dimensional large-scale wind field can be considered partially by the specification of spatially constant gradients $\partial v_g/\partial y$ and $\partial\Theta/\partial y$ which are related to the cross-front geostrophic deformation and shear field by the continuity equation $\partial u_g/\partial x = -\partial v_g/\partial y$ and the equation of thermal wind balance $\partial u_g/\partial p = -\gamma\, \partial\Theta/\partial y$, respectively. ($\gamma = g/(f\Theta)$, g = gravity acceleration, f = Coriolis parameter).

The inclusion of these terms in the model equations is essential for the simulation of fronts, because they determine the geostrophic forcing of the cross-front ageostrophic circulation, including vertical velocity, and thus crucially influence the frontal development, especially the evolution of clouds and precipitation: The disturbance of the thermal wind balance in the frontal area by the geostrophic shear or deformation field drives an ageostrophic circulation which again restores the balance. The tendency of the disturbance of the thermal balance is given by the Q-vector (eq. (1) in BHRT95) and the divergence of the Q-vector is the forcing term for the vertical velocity (described by the omega-equation, see Hoskins et al., 1978). In the observed case of 9 May 1989 the comparison of the spatial distribution of the divergence of Q_n (the component normal to the isentropes) and of the relative humidity in 850 hPa height (Fig. 4 in BHRT95) indicates that the geostrophic forcing is essential for the development of the broad frontal cloud band.

Due to the limitations of the two-dimensional model only the divergence of the component of the Q-vector in the model plane Q_1, which is almost equal to Q_n, is accounted for in the simulations:

$$Q_1 = \frac{g}{\Theta}\left(\frac{\partial v_g}{\partial x}\frac{\partial\Theta}{\partial y} + \frac{\partial u_g}{\partial x}\frac{\partial\Theta}{\partial x}\right). \qquad (1)$$

In this case study the confluence term $\partial u_g/\partial x\ \partial\Theta/\partial x$ is the most important forcing term. $\partial u_g/\partial x$ reaches a value of $-2\cdot 10^{-5}\ \mathrm{s}^{-1}$ ($\Delta u = 10$ m/s over a distance of 500 km, derived from ECMWF analyses) at 12 UT in the vicinity of the front. A constant value of $\partial u_g/\partial x = -1.5\cdot 10^{-5}\ \mathrm{s}^{-1}$ and $\partial u_g/\partial z = 0$ was assumed to be representative during the simulation.

The ECMWF analyses do not provide any details on a scale smaller than 200 km. Thus the mesoscale initial state was derived from the sequence of radio soundings at the Island Helgoland, 50 km ahead of the coast (Fig. 8 in BHRT95). Assuming a constant frontal speed of 6 m/s the 3 h time interval between the soundings corresponds to a horizontal distance of 65 km. Nevertheless the initial potential temperature field Θ and the along front wind field v must be in geostrophic balance. The wind field v shows more details than the Θ-field and therefore it was chosen as the primary field from which Θ was derived by horizontal integration of the thermal wind equation. The value of the constant term of the integration in each layer was chosen so that the calculated and the observed temperature coincided in the vicinity of the front according to a least square fit. Before applying the thermal wind equation the v-field was averaged over a vertical distance of 1000 m and a horizontal distance of 50 km in order to obtain smooth fields and to prevent the occurrence of potential unstable areas in the derived Θ-field. The specific humidity field was derived from the Helgoland soundings as well, and smoothed in the same way as v. The wind speed u in the model plane was not derived from the measurements but was chosen equal to the geostrophic wind with a superposed ageostrophic circulation calculated from the Sawyer-Eliassen equation in order not to excite gravity waves.

4. The front over the sea surface

The most striking feature of the front over the sea observed on 9 May 1989 was the presence of

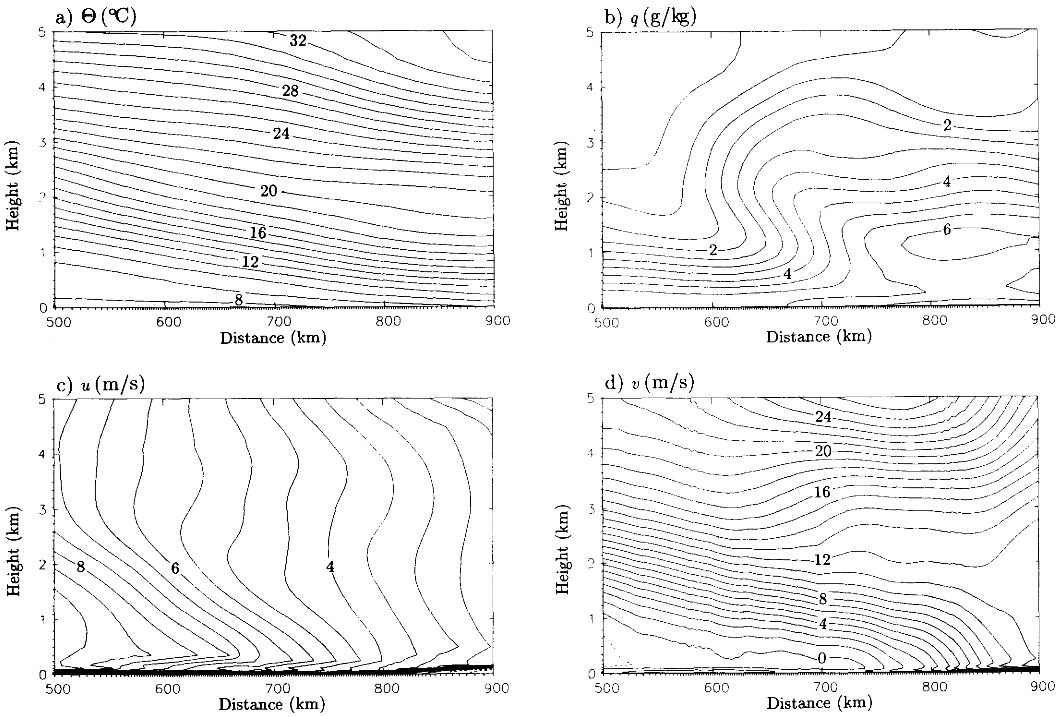

Fig. 1. Initial fields of potential temperature Θ (a), specific humidity q (b), cross-front wind speed u (c) and along-front wind speed v (d) in the numerical simulation of the front over the sea.

several narrow cloud-bands at the leading edge of the front, which are clearly visible in the satellite images (Fig. 1 in BHRT95) and were reported by the aircraft observers. The narrow cloud bands were followed by a broad cloud band at higher levels. The development of these cloud bands is investigated here by means of numerical simulations. The strategy is to initialize the frontal structure on a larger scale and to allow the evolution of the small-scale patterns.

Fig. 1 shows the initial fields of Θ, q, u and v in a part of the model domain. The whole model domain at first extends from $x = 0$ to $x = 1200$ km and up to $z = 15$ km. The outward pointing marks at the figure boundaries indicate the positions of the grid points. Their horizontal distance in the highly resolved area between 600 and 800 km is 2 km and the vertical distance is less than or equal to 150 m everywhere below 4000 m height in order to allow small scale patterns to evolve. The model domain is moved relative to the ground with a speed of 4.5 m/s. Thus the front remains almost stationary in the highly resolved area.

The initial fields Θ, q and v (Fig. 1a, b, d) were derived from 3-hourly radio soundings launched on the island Helgoland. They differ from the fields presented in Fig. 8 of BHRT95 because they have been smoothed according to the procedure described in the previous section in order to obtain stable and consistent fields. The frontal zone is characterized by a broad baroclinic zone (Fig. 1a) correlated with the horizontal and vertical shear zone of the along-front wind component (Fig. 1d). The initialized fields do not show any structure on a scale smaller than 50 km. The ageostrophic cross-front circulation in the initial state derived from the Sawyer-Eliassen equation results in a thermally direct circulation that is superposed on the deformation field (Fig. 1c). This cross-front wind field is consistent with the specific humidity field derived from the observations (Fig. 1b), with a prefrontal moisture maximum and a post-frontal moisture minimum. The initial relative humidity maximum is 93%. Thus clouds are absent in the initial state. The sea-surface temperature is constant in time but varies horizontally. It is equal to

8°C for $x < 600$ km but has a constant gradient for $x > 600$ km and reaches 12°C at $x = 1200$ km. This corresponds approximately to the observed sea-surface temperature which increased towards the coast. Thus the air is heated from below since the front moves towards higher values of the sea-surface temperature.

The numerical simulation is performed for 24 h. Three stages of the frontal development can be distinguished: during the first 6 h of simulation the prefrontal air is simply lifted by the ageostrophic circulation without any cloud generation.

The second stage is characterized by the first occurrence of saturation after 6 h of simulation

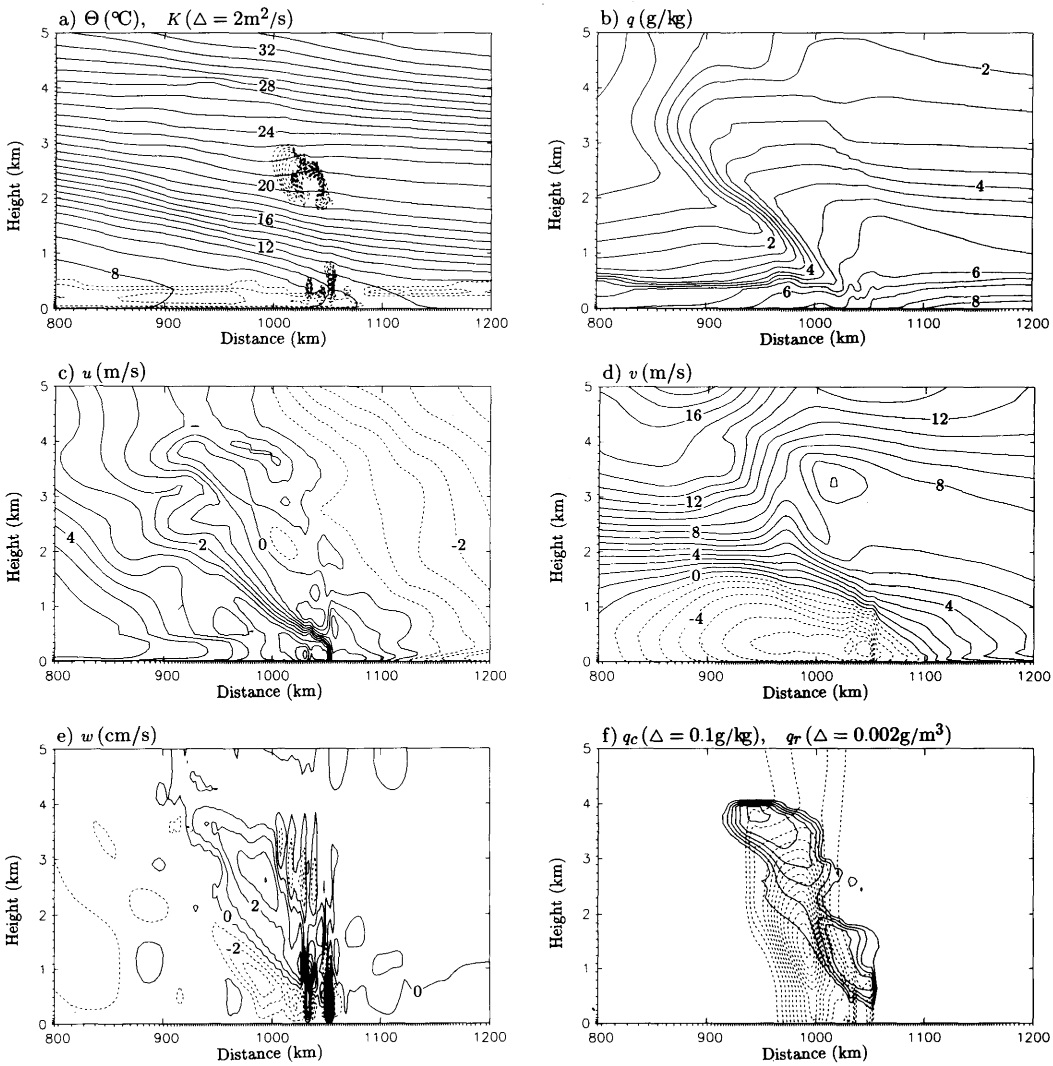

Fig. 2. Fields of potential temperature Θ (a, solid lines), exchange coefficient for momentum K (a, dashed lines), specific humidity q (b), cross-front wind speed u (c), along-front wind speed v (d), vertical velocity w (e), cloud water content q_c (f, solid lines) and rain water content q_r (f, dashed lines) after 21 h of the numerical simulation of the front over the sea with a horizontal sea-surface temperature gradient. Although the computational domain is moved with a speed of 4 m/s, the horizontal distances in Figs. 1 to 4 are given in the stationary coordinate system fixed to the ground.

between 2000 and 2500 m height and by the subsequent development of a compact cloud in the moist potential unstable environment. The cloud top raises up to 3500 m height until 9 h of simulation and the vertical velocity in the updraft remains larger than 10 cm/s until 15 h of simulation. At this time the moist potential instability in the cloud area has almost disappeared due to the vertical displacement of the air masses by the resolved updraft and the parameterized turbulent exchange. So far the simulation has to be regarded as an adaptation process to a balanced state rather than a realistic simulation of the frontal development.

The 3rd stage lasts from 15 h to the end of the simulation at 24 h. At 15 h, a balanced state is achieved and further on the cloud area is only slightly lifted by the ageostrophic circulation. Fig. 2 shows the frontal state after 21 h of simulation. The cold and dry air below the cloud is cooled by the evaporating precipitation (Fig. 2f) and therefore the ageostrophic circulation is enhanced below 2000 m height (Figs. 2c, e). The largest cross-front flow and subsidence is found behind the surface front in the area below the compact cloud. Because of this strong cross-front circulation at low levels a second maximum of cloud water content develops at 1000 m height in the moist and warm air which is ascending on top of the frontal inversion. In this cloud region the stratification is stable almost everywhere. The dashed lines in Fig. 2a show the turbulent transfer coefficient K. Values different from zero indicate areas of potential instability or moist potential instability, respectively, if saturation is reached. Outside the boundary layer there is only one unstable region between 2000 and 3000 m height with an alternating vertical velocity pattern of 1 to 2 cm/s (Fig. 2e), but the amount of cloud water in this area is weak (Fig. 2f). There is a further cloud area at 6000 m height (outside the scope of the figures) with weak precipitation and only small influence on the frontal development.

In the unstable boundary layer convection emerges in form of two convergence lines with vertical velocities up to 10 cm/s. The first convergence line developed after 12 h of simulation ahead of the precipitation area. It was enforced after 16 h of simulation when saturation was reached in the boundary layer and moist potential instability occurred. After 20 h of simulation a second convergence line evolved 20 km behind the first one. Both lines are well established after 21 h of simulation (Fig. 2e) at 1050 and 1030 km. They move forward relative to the compact cloud area aloft because of the enhanced secondary circulation at low levels. The movement of the two convergence lines can be traced by the temporal development of temperature T and cross-front wind u at 10 m height (Fig. 3). The frontal zone is characterized by an area of enhanced horizontal temperature gradient on a scale of 100 km (Fig. 3a) with an area of convergent cross-front wind ahead of it. Embedded in the broad frontal zone two strong convergence lines develop on a scale of 10 km each (Fig. 3b) which are correlated with maxima in the temperature gradient. They move forward relative to the large scale gradients. The leading convergence line dissolves during the simulation. After 24 h of simulation it has just vanished, but at that time there is already a third line developing behind the second line.

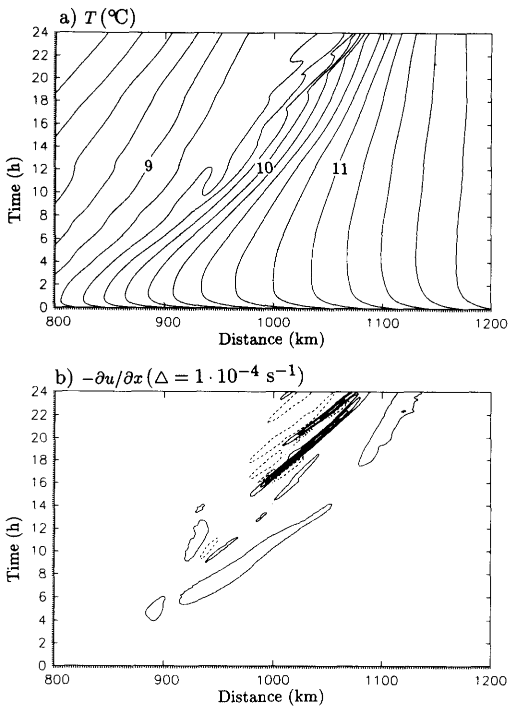

Fig. 3. Time development of temperature T (a) and convergence of the cross-front wind component $-\partial u/\partial x$ (b) at 10 m height in the simulation of the front over the sea with a horizontal sea-surface temperature gradient.

The simulation clearly shows the effect of the ageostrophic circulation forced by the geostrophic convergence field. The cross-front circulation causes the evolution of the broad cloud band in the upgliding warm air and the dry tongue in the sinking cold air. The strong specific humidity gradients below the upgliding moist air and on top of the postfrontal boundary layer which were present in the observation (Fig. 8a in BHRT95) but smoothed in the initial field (Fig. 1b) are enhanced again after 21 h of simulation (Fig. 2b).

The numerical simulation does not distinguish between cloud bands. It merely shows several updrafts and precipitation maxima inside a broad cloud area. Nevertheless, there is a lot of correspondence with the observations, if the low-level updrafts and precipitation maxima in the simulation are identified with the cloud bands observed by the satellites. Furthermore, the u and q patterns in the simulation show similarities to the patterns derived from the aircraft measurements below 1500 m. The observed cross-front wind field u (Fig. 9b in BHRT95) indicates two convergence lines at $x = 130$ and $x = 230$ km. The latter is characterized by gradients $\partial u/\partial x < 0$ (convergence) below 500 m and positive gradients (divergence) at 1000 m height. They are correlated with maxima in the specific humidity visible in the shape of the 6 g/kg-isoline (Fig. 9a in BHRT95). Between $x = 270$ and $x = 370$ km a tilted convergence zone was observed below the broad specific humidity maximum. Corresponding patterns in the simulation can be found at $x = 1030$, 1050 and between 1050 and 1100 km in Fig. 2b, c, although the scale of the patterns in the simulation is smaller than in the observation. The correspondence is not as good in v, there the simulated field is relatively smooth. Furthermore, there are some discrepancies in the large-scale fields. The values of u and v in the vicinity of the surface front after 21 h of simulation are smaller than observed although they have been initialized with reasonable values. The reduction of u and v during the simulation is a consequence of the ageostrophic cross-front circulation: The cross-front wind u decreases because the surface front moves forward into an area with a smaller geostrophic wind component u_g and the along-front geostrophic wind decreases because of the intensification of the horizontal temperature gradient aloft. According to the thermal wind equation this implies a lower along-front wind component below.

The sensitivity of the development of the low-level convergence lines to the heating from below, caused by the movement of the front towards an area of higher sea-surface temperature is investigated in a further simulation with a homogeneous sea surface temperature of 8°C: In that case there is almost no moist potential instability found in the boundary layer and after 21 h of simulation the surface front shows less mesoscale structures below 1000 m height. Only one weak convergence line with an updraft of 3 cm/s develops in the boundary layer.

Fig. 4 shows horizontal traces of temperature T and precipitation rate r through the front at 10 m height for both simulations with and without a sea-surface temperature gradient. In the first case the compact cloud area at mid-levels and the convergence lines in the boundary layer are sources of three rain bands, resulting in precipitation maxima at the ground. At the surface front there is an overall temperature drop of about 1 K at 10 m height.

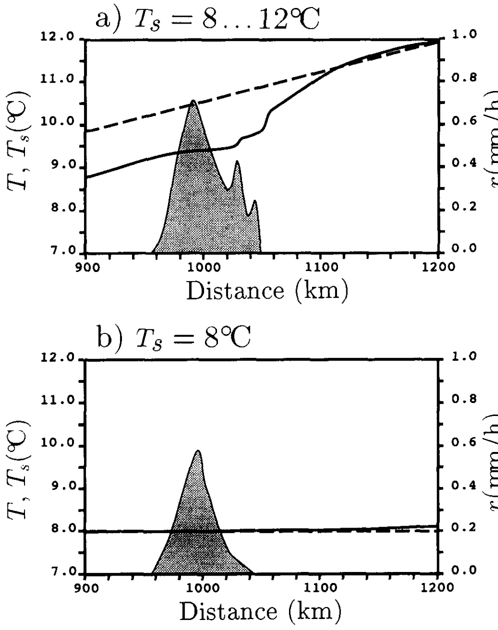

Fig. 4. Traces of air temperature T (solid line), sea-surface temperature T_s (dashed line), and precipitation rate r (shaded) at 10 m height after 21 h of the simulation of the front over the sea with (a) and without (b) a horizontal sea-surface temperature gradient.

In the second case with a homogeneous sea-surface temperature only one broad precipitation area develops without any structure. A strong temperature gradient is missing. The temperature difference is only 0.3 K over a distance of 500 km. This sensitivity study confirms that a constant sea surface temperature reduces the thermal differences near the ground and prevents the development of strong surface fronts. Nevertheless a distinct temperature drop emerges if the sea surface temperature has a weak gradient. The stronger temperature gradient at the surface front develops from the pre-existing weak temperature gradient (due to the inhomogeneous surface temperature) and the confluent and therefore frontogenetic flow.

Thus the observed low-level convergence lines correlated with the thin cloud bands are probably caused by the inhomogeneous sea surface temperature.

4. The front over the land area

The front observed on 9 May 1989 experienced distinct modifications when it passed the coast as described in BHRT95. Especially the satellite images show a transformation of the cloud bands: The narrow cloud bands at the leading edge of the front weakened and disappeared when they reached the coast. Over land small cumulus clouds developed in the heated boundary layer in the morning. At noon, a compact cloud band evolved just behind the coast and moved inland with an cloud-free area behind it.

The modifications were also visible in the surface observations. The front was characterized by a broad baroclinic zone at Helgoland 50 km ahead of the coast, but a sudden temperature drop and wind direction change caused by the sea-breeze front was present in Nordholz, only 10 km behind the coast. Also further inland only one frontal event was observed. Thus the synoptic-scale cold front and the sea-breeze front must have merged. These processes are further investigated in this section.

In this simulation the model domain is not moved with the front, but fixed to the ground. For $x > 0$ km a land surface with a surface temperature which is treated as a prognostic variable is considered, whereas the sea-surface temperature is constant at 8°C for $x < 0$. The horizontal resolution is 2.5 km everywhere over the land. The vertical resolution is finer than in the previous simulations in order to resolve the shallow circulation patterns of the sea-breeze in the morning, when the boundary-layer height is small. The vertical resolution is less than 100 m below 1000 m height and less than 25 m below 500 m.

In the previous section the simulation of the front over the sea yielded a frontal state with similar mesoscale patterns as observed. Nevertheless, this state could not be taken as the initial state of this simulation because the large scale values of u and v in the vicinity of the front departed considerably from the observed values at the time the front passed the coast.

Thus the initial fields of this simulation (Fig. 5) are derived from the observations in the same way as in the previous one. There are slight differences because the initialization procedure was changed in order to achieve a better representation of the low-level prefrontal inversion, which is important for a realistic simulation of the boundary-layer growth and the sea-breeze evolution in the morning: The interval used to average v vertically was decreased from 1000 m to 500 m and the location where the derived temperature field was fitted to the observed field was shifted further to the warm side of the front.

At 06 LT (local time) the observed surface temperatures and the vertical distributions of Θ in the boundary layer were almost the same over the sea and the land. Thus 06 LT was taken as the starting time of the simulation. In order to compare with the times given in the observational part, half an hour must be added to the times given in UT.

The broad frontal zone, characterized by the horizontal temperature gradient (Fig. 5a) and wind shear (Fig. 5d) is located about 100 km ahead of the coast. The broad prefrontal humidity maximum is located in the coastal area (Fig. 5b). The deformation field $\partial u/\partial x$ is $-1.5 \cdot 10^{-5}$/s as in the previous simulations. The absolute value of u_g is chosen so that the on-shore geostrophic wind is 3 m/s at the coast (Fig. 5c). Nevertheless the superimposed ageostrophic circulation causes higher on-shore wind speeds outside the boundary layer. The low-level along-front wind maximum is located just at the coast (Fig. 5d). It is geostrophically balanced outside the boundary layer and thus

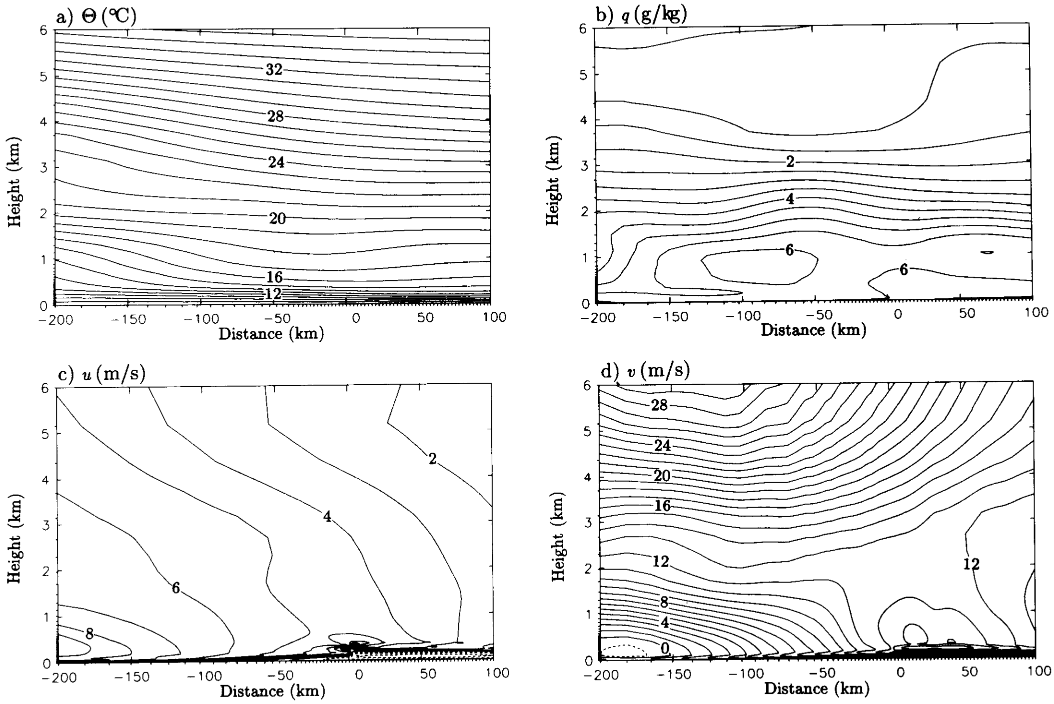

Fig. 5. Initial fields of potential temperature Θ (a), specific humidity q (b), cross-front wind speed u (c), along-front wind speed v (d) in the numerical simulation of the front passing the coast.

corresponds to a horizontal pressure gradient maximum $\partial p/\partial x > 0$ which causes a distinct offshore flow $u < 0$ below the boundary layer inversion (Fig. 5c). The pressure minimum at the ground is found 150 km offshore. In contrast to the previous simulation, this study does not deal with the mesoscale features which slowly evolve from a prescribed large scale field, but focuses on the development of the sea breeze front in the prefrontal environment. For this purpose, no adaptation process must be accounted for.

Fig. 6 shows the time development of the meteorological parameters at 10 m height. Four stages of development can be distinguished: (i) the development of a coastal front from 06 until 09 LT, characterized by an increasing temperature gradient at the coast (at $x = 0$) (Fig. 6a); (ii) the evolution of a sea-breeze front moving inland after 09 LT with positive values of cross-coast wind speed u behind the front (Fig. 6c) and a distinct wind shear in the along-coast component v (Fig. 6d); (iii) the modification of the sea-breeze front by deep convection accompanied by precipitation after 13 LT, causing a specific humidity maximum behind the front (Fig. 6b); and (iv) the dissolution of the distinct surface front in the late evening after 20 LT visible in all parameters. The state of the front is now further investigated at 09, 12 and 15 LT. Vertical cross-sections of potential temperature Θ and cross-front and cross-coast wind speed u are presented. They show the thermal forcing and the dynamic response of the sea breeze circulation. The top of the turbulent boundary layer (exchange coefficient $K = 1$ m^2/s) is indicated as well, in order to show the area where frictional forces are important. In some cases the along-front wind v, specific humidity q, cloud water q_c and rain water q_r are shown in order to illustrate the state of the synoptic-scale front and the diabatic forcing.

Fig. 7 shows the state at 09 LT when the coastal front is well established, just before it starts to move inland. The boundary layer over land has increased to 500 m height due to the heating of the ground (Fig. 7a). In spite of the on-shore

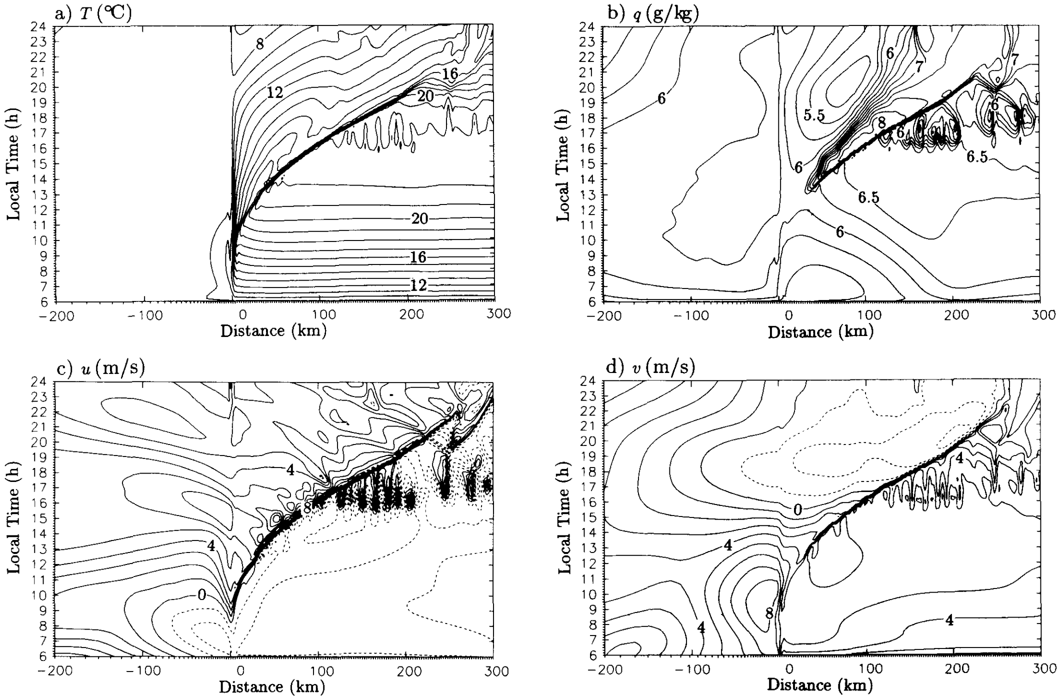

Fig. 6. Time development of temperature T (a), specific humidity q (b), cross-front wind u (c) and along-front wind v (d) at 10 m height in the simulation of the front passing the coast.

geostrophic wind component u_g there is still an offshore wind u (Fig. 7b) in the boundary layer. Just ahead of the coast near the sea surface a baroclinic zone has developed due to the advection of the warm boundary-layer air over the sea (Fig. 7a). At the ground there is a distinct temperature difference of $5K$ exactly at the coast due to the strong coastal convergence. The density contrast causes a pressure difference that amounts to 0.3 hPa. This pressure gradient forces a shallow on-shore flow of 100 m height just at the coast (Fig. 7b), which increases with time and later becomes the feeder flow of the sea-breeze front (Fig. 6c). The coastal front is a boundary-layer effect which is confined to the layer below 500 m height and thus has nearly no effect on the synoptic-scale cold front. Nevertheless, the gradients at the ground are much stronger than those of the synoptic-scale front. The broad frontal zone is still about 100 km offshore. Its appearance has not changed much with respect to the initial state in Fig. 5.

The offshore boundary-layer flow cannot sustain the increasing pressure gradient at the coast and thus the sea-breeze front leaves the coast between 09 LT and 10 LT and moves inland (Fig. 6). At 12 LT (Fig. 8) it is located 25 km behind the coast and moves inland with a speed of 3.5 m/s with a feeder flow of 7 m/s just behind it (Fig. 8b) and an updraft of $w = 38$ cm/s in front of its head. Thus it shows the characteristics of a density current. The vertical velocity is the mean over the mesh size of $\Delta x = 2.5$ km and the width of the updraft is limited by the resolution. The maximum w value would be even higher if Δx were smaller. The reverse flow on top of the feeder flow is confined to a height of 1500 m which is approximately the height of the boundary layer over land. The influence of the sea-breeze front on the environment is confined to this height. The air in the feeder flow behind the front stems from the cold air below the shallow inversion over the sea surface and not from the cold air mass behind the synoptic-scale cold front which is still 50 km apart from the coast. The feeder flow is heated by the land surface and by the entrainment

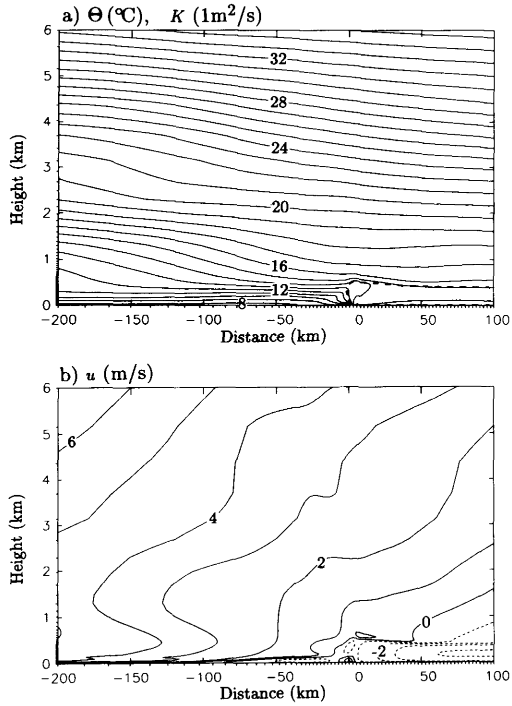

Fig. 7. Fields of potential temperature Θ (a, solid lines), exchange coefficient for momentum K in excess of 1 m^2/s (a, dashed line), and cross-front wind speed u (b) at 09 LT in the numerical simulation of the front passing the coast.

of warmer air from above. Thus a moderate temperature gradient develops between the coast and the sea-breeze front and a stronger gradient is found in the convergence zone at the frontal head (Fig. 6a, 8a). The pressure at the ground shows a corresponding behavior with a sudden rise of approximately 1 hPa at the sea-breeze front and a continuous increase between the sea-breeze front and the coast. The synoptic-scale cold front is still located 50 km off the coast, visible in the potential temperature gradient $\partial\Theta/\partial x$ above the boundary layer (Fig. 8a) and the shear in the along-front wind component (Fig. 8c). There is still a moderate updraft of 3 cm/s in the coastal area which generated a cloud at 2000 m height, resulting in an area of weak moist potential instability (enclosed by a dashed line in Fig. 8a).

After 12 LT condensation occurs in the updraft at the sea-breeze front and convection extends up to 5000 m height at 15 LT (Fig. 9b). A compact

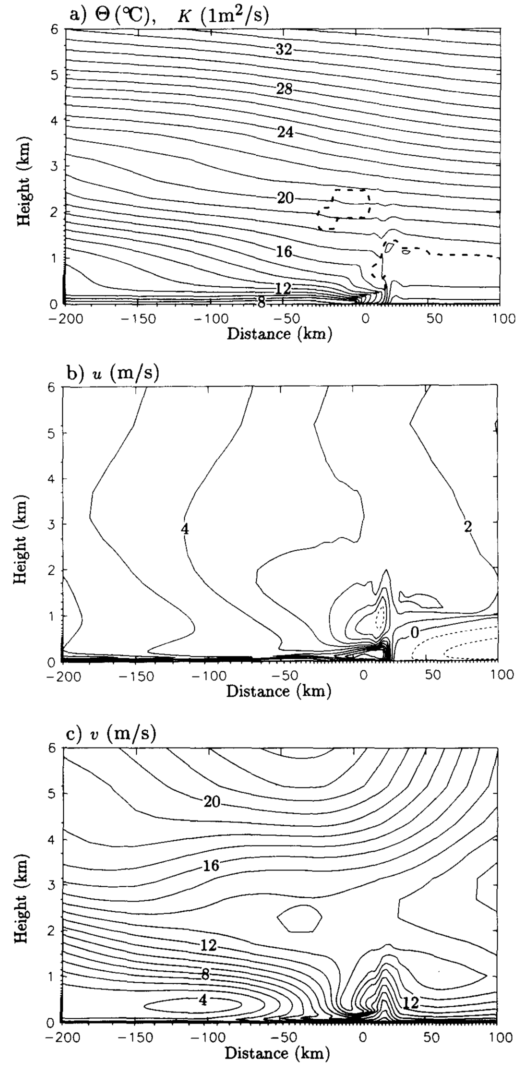

Fig. 8. Fields of potential temperature Θ (a, solid lines), exchange coefficient for momentum K in excess of 1 m^2/s (a, dashed line), cross-front wind speed u (b), and along-front wind speed v (c) at 12 LT in the numerical simulation of the front passing the coast.

precipitating cloud band has developed, which is separated into a narrow cold-frontal rainband of 10 km width with a strong updraft of 3 m/s at the surface front and a broader cloud of 40 km width behind it. The ageostrophic circulation (Fig. 9c) now extends about 100 km seawards and causes sinking motion at the coast. The cloud which was previously located at the coast disappeared. Thus,

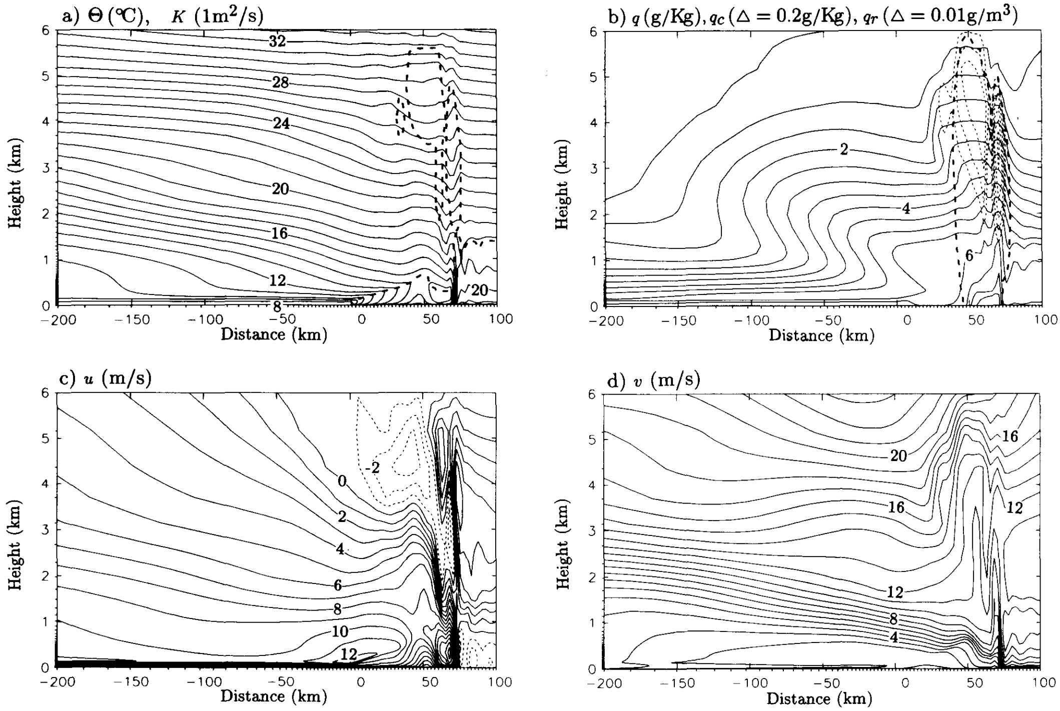

Fig. 9. Fields of potential temperature Θ (a, solid lines), exchange coefficient for momentum K in excess of 1 m^2/s (a, dashed line), specific humidity q (b, solid lines), cloud water content q_c (b, thin dashed lines), rain water content in excess of 0.01 g/m^3 (b, thick dashed line), cross-front wind speed u (c), and along-front wind speed v (d) at 15 LT in the numerical simulation of the front passing the coast.

this ageostrophic circulation may be responsible for the cloud gap behind the compact cloud band at the front observed in BHRT95. There is a strong ageostrophic on-shore flow at the coast (Fig. 9c) and the synoptic front and the sea-breeze front have merged in the convergence zone. The along-front wind minimum at low levels, which was located beyond the inversion of the synoptic-scale front now almost extends to the sea-breeze front (Fig. 9d) due to advection and due to the decrease of v by the Coriolis force in the ageostrophic cross-front flow $u > U_g$. The anomalies in the wind and temperature fields in the area 20 km behind the front are caused by the cold-air outflow in the precipitation area. Behind the sea-breeze front the precipitation rate at the ground amounts 18 mm/h. The postfrontal dry air is cooled by evaporation; A temperature minimum and pressure maximum is generated just behind the front and the frontal temperature, pressure and specific humidity difference is enhanced. A separated pressure minimum correlated with the synoptic-scale cold front is not present any more in this stage of the development.

In the evening at 21 LT several updrafts with clouds and precipitation developed ahead and behind the density current as well. They exhibit low-level outflows of cold air both in $+x$ and $-x$ direction (Fig. 6c). The distinct front is still present at $x = 230$ km in the vertical cross-sections (not shown) but the frontal gradients at the ground have weakened considerably (Fig. 6).

This simulation describes the evolution of a sea-breeze front and its merging with the synoptic-scale front consistent with the observations. It shows many similarities to a situation investigated by Physick (1988) also by means of numerical simulation. There, a synoptic-scale front which approached the coast was accelerated by the coastal pressure gradient due to the heating of the land surface. But in our simulation a much smaller grid size is used so that the processes on the meso-γ scale, which are characteristic for sea-breezes, could be resolved.

The question remains if the sea-breeze front developed independently of the synoptic-scale front or was merely triggered by it. Usually sharp sea-breeze fronts are not observed directly behind the coast under on-shore wind conditions, but sometimes develop about 50 km inland (Simpson et al., 1977). Nevertheless a sharp surface front is present 10 km behind the coast in the observational case study of 9 May 1989. The strong front owes its existence to the generation of a coastal front by the frictional convergence in the early morning as shown by the simulation. This case study is characterized by a large along-coast geostrophic wind component v_g of 15 m/s ahead of the synoptic-scale front. This corresponds to a pressure gradient that causes a seawards directed flow in the boundary layer over the land surface. Roeloffzen et al. (1986) showed, that the conditions met in this case study, namely a strong along-coast geostrophic flow v_g and a weak on-shore flow u_g favor the generation of a coastal front. These findings are confirmed by further simulations with this model (not shown): If a horizontal homogeneous initial state similar to the prefrontal conditions of this case study is chosen, a sea-breeze front develops without presence of a synoptic-scale front. Thus, it can be stated that the onset of the sea-breeze front in the morning of 9 May 1989 was not directly related to the approaching synoptic-scale front, but merely to the conditions in the prefrontal environment.

Later in the course of the day the two frontal systems merged. This development was obviously enhanced by the evolution of deep convection triggered by the sea-breeze front in the area of high relative humidity ahead of the synoptic-scale front. The sensitivity to the humidity was further investigated by a simulation carried out without consideration of moisture processes. Up to 12 LT, the results are very similar to the reference simulation because saturation rarely occurred up to this time, but at 15 LT the differences are significant. Whereas deep convection occurred in the reference simulation, the ageostrophic circulation is confined below a height of 2000 m in the dry run. A reverse flow between 1000 and 2000 m height and the downdraft 50 km behind the sea-breeze front counteract the approaching synoptic-scale front. The synoptic-scale front is rather retarded than accelerated by the sea-breeze circulation if no condensation occurs. Thus the presence of high relative humidity and conditional potential instability in the prefrontal area was important for the strengthening of the sea-breeze front and the merging of the two fronts stemming from different scales.

5. Summary and conclusions

The numerical simulations presented in this study give a detailed description of a cold front similar to the front observed over the North Sea and over northern Germany during the field experiment FRONTEX 89. The simulations figure out the processes which are responsible for the development of the observed mesoscale cloud bands over sea and the modification of the synoptic-scale front over the land due to the interaction with a sea-breeze front.

The ageostrophic cross-front circulation forced by the geostrophic deformation field caused the observed field of specific humidity. A moisture maximum ahead of the front and a tongue of dry air behind it. This pattern is commonly observed at cold fronts and was very pronounced in this case study. Over the sea convergence lines evolved in the unstable boundary layer in the broad frontal zone. They moved forward relative to the front due to the ageostrophic circulation that was enhanced at low levels due to the cooling of the cold and dry air by evaporation of the rain stemming from the upgliding warm and moist air.

This simulation confirms the findings that a homogeneous sea surface temperature generally smoothes the frontal contrasts near the surface and suppresses the evolution of sharp surface fronts. Nevertheless other mechanisms may counteract the frontolytic effect. In this simulation the gradient of the sea-surface temperature caused a frontogenetic effect in the confluent wind field. In a previous case study (Hennemuth et al., 1992) the temperature contrast of a front over the sea was maintained by differential cooling due to longwave radiation divergence.

At the coast a sea-breeze front developed. Its horizontal gradients of Θ, q, u and v at the ground were much larger than those of the synoptic-scale cold front because of the smaller scale of the sea-breeze front and the larger temperature differences involved, due to the strong land-sea contrast. Over the land, the passage of the sea-breeze front was the main frontal event observed at the surface, but the synoptic-scale cold front remained unchanged outside the boundary layer until noon. The two frontal systems did not merge until the vertical scale of the sea-breeze front increased considerably in the afternoon, due to the evolution of deep convection, which was triggered by the sea-breeze front in the moist conditionally unstable environment.

The observations of the front of 9 May 1989 (BHRT95) and the related simulations presented in this paper illustrate the modification of a front, which was caused by a change of the conditions of the underlying surface. This case study emphasizes the influence of the lower boundary conditions and of the turbulent heat and momentum fluxes in the boundary layer on the mesoscale characteristics of surface fronts.

The basic characteristics of the observed front are reproduced in the numerical model. This success is a consequence of its special features, adopted to the purpose of frontal simulations, namely the high resolution in the boundary layer and at the surface front, achieved by the non-equidistant grid and the consideration of the geostrophic deformation and shear terms, which are important for frontal development. Nevertheless there are some deficiencies.

The model does not yield separated cloud bands as observed by the satellites over the sea, but produces convergence lines and rainbands inside a broad cloud area. This may be caused by the relatively simple Kessler scheme used to parameterize the cloud processes. Furthermore the scale of the cloud bands, its horizontal distance and its vertical extension, is underestimated by a factor 2. This also may be a reason for the missing cloud gaps because the circulations did not become deep enough to produce its own downdrafts.

The wind speeds after 24 h of simulation did not correspond well with the observed values. During this period the frontal state was exposed to the large-scale deformation field which caused the changes in wind speed in the frontal area. Suitable initial fields were not available 24 h before the observation, but this time was required for the adaption to a balanced state and the development of the mesoscale cloud bands. Furthermore the effect of along-front variations are not negligible on this time scale. Nevertheless, they must be neglected in a 2-dimensional model.

In the simulation of the front over land, the strength of the convection and the amount of precipitation is overestimated. There was no observation of rain in the first 100 km behind the coast whereas the model produced heavy precipitation. This was due to the fact that the simulation was started without clouds. A maximum relative humidity value of 93% was derived from the radio-soundings. The first occurrence of saturation in the simulation caused the release of moist potential instability. Strong convection took place until a balanced state was achieved. Maybe the amount of conditional potential instability was overestimated in the initial state, because the vertical temperature gradient was not derived directly from the measurements but modified in order to ensure the thermal balance with the observed wind field. Nevertheless the observed sea-breeze front was accompanied by a compact cloud band and thunderstorms were reported in the night.

The deficiencies of the simulations can be mainly contributed to the difficulties of representing the three-dimensional flow in the two-dimensional model and obtaining a suitable initial state, so that the resulting temporal development remains consistent with the observations over a longer time interval and spin-up problems are avoided.

It is difficult to overcome the restrictions of the two-dimensional model while maintaining the high resolution necessary to resolve the mesoscale patterns in the frontal area, because of the high demands of three-dimensional simulations on computer resources. Maybe this purpose can be achieved by nested models or adaptive grids.

The problem of choosing an appropriate initial state is a very general problem of numerical simulations, performed in order to interpret observational data. The observations during field experiments are distributed in space and time. The procedure of finding a suitable initial state on the appropriate scale usually is that of trial and error. This situation may change in the future, when variational four-dimensional data assimilation schemes become available, allowing the determination of a spatial and temporal consistent atmospheric state fitted to the data.

6. Acknowledgements

This study was sponsored by the Deutsche Forschungsgemeindschaft. I thank Prof. B. Brümmer and Dr. B. Hennemuth for discussions and many suggestions.

7. Appendix

7.1. Model equations

The non-hydrostatic model consists of prognostic equations for potential temperature Θ, specific humidity q, cloud water content q_c, rain water content q_r, and the wind components u, v and w:

$$\frac{\partial \Theta}{\partial t} = -u\frac{\partial \Theta}{\partial x} - v\frac{\partial \bar{\Theta}}{\partial y} - w\frac{\partial \Theta}{\partial z} + \frac{\partial}{\partial x}K_h \times \frac{\partial \Theta}{\partial x} + \frac{\partial}{\partial z}K_h\frac{\partial \Theta}{\partial z} + \frac{L}{c_p}(C + C_r), \tag{A.1}$$

$$\frac{\partial q}{\partial t} = -u\frac{\partial q}{\partial x} - w\frac{\partial q}{\partial z} + \frac{\partial}{\partial x}K_h \times \frac{\partial q}{\partial x} + \frac{\partial}{\partial z}K_h\frac{\partial q}{\partial z} - C - C_r, \tag{A.2}$$

$$\frac{\partial q_c}{\partial t} = -u\frac{\partial q_c}{\partial x} - w\frac{\partial q_c}{\partial z} + \frac{\partial}{\partial x}K_h \times \frac{\partial q_c}{\partial x} + \frac{\partial}{\partial z}K_h\frac{\partial q_c}{\partial z} + C - T_a - T_c, \tag{A.3}$$

$$\frac{\partial q_r}{\partial t} = -u\frac{\partial q_r}{\partial x} - (w + w_f)\frac{\partial q_r}{\partial z} + \frac{\partial}{\partial x}K_h \times \frac{\partial q_r}{\partial x} + \frac{\partial}{\partial z}K_h\frac{\partial q_r}{\partial z} + C_r + T_a + T_c, \tag{A.4}$$

$$\frac{\partial u}{\partial t} = -u\frac{\partial u}{\partial x} - w\frac{\partial u}{\partial z} + f(v - v_g) + u_g\frac{\partial u_g}{\partial x} - \frac{1}{\bar{\rho}}\frac{\partial (p' + p'')}{\partial x} + \frac{\partial}{\partial x}K_m\frac{\partial u}{\partial x} + \frac{\partial}{\partial z}K_m\frac{\partial u}{\partial z}, \tag{A.5}$$

$$\frac{\partial v}{\partial t} = -u\frac{\partial v}{\partial x} - v\frac{\partial v_g}{\partial y} - w\frac{\partial v}{\partial z} - f(u - u_g) + v_g\frac{\partial v_g}{\partial y} + \frac{\partial}{\partial x}K_m\frac{\partial v}{\partial x} + \frac{\partial}{\partial z}K_m\frac{\partial v}{\partial z}, \tag{A.6}$$

$$\frac{\partial w}{\partial t} = -u\frac{\partial w}{\partial x} - w\frac{\partial w}{\partial z} - \frac{1}{\bar{\rho}}\frac{\partial p''}{\partial z} + \frac{\partial}{\partial x}K_m\frac{\partial w}{\partial x} + \frac{\partial}{\partial z}K_m\frac{\partial w}{\partial z}, \tag{A.7}$$

with Coriolis parameter f, gas constant R, specific heat c_p of dry air and latent heat of evaporation L. K_h and K_m are the turbulent exchange coefficients for heat and momentum. C, C_r are condensation rates, and T_a, T_c are transition rates from cloud water to rain water, respectively.

The three wind components have to fulfill the continuity equation in the anelastic approximation:

$$\bar{\rho}\frac{\partial}{\partial x}u + \bar{\rho}\frac{\partial}{\partial y}v_g + \frac{\partial}{\partial z}\bar{\rho}w = 0. \tag{A.8}$$

The thermodynamic fields of Θ and density ρ are split into a large scale part ($^-$) and a mesoscale part ($'$): $\Theta = \bar{\Theta} + \Theta'$, $\rho = \bar{\rho} + \rho'$. The pressure p additionally consists of a correction term p'' which enforces the continuity equation to be fulfilled: $p = \bar{p} + p' + p''$. The large scale fields $\bar{\Theta}$, $\bar{\rho}$ and $\bar{p}$ are independent of x and t and fulfill the hydrostatic equation and the equation of state:

$$\frac{\partial}{\partial z}\bar{p} = -g\bar{\rho}, \qquad \bar{p} = \bar{\rho}R\left(\frac{\bar{p}}{p_0}\right)^{R/c_p}\bar{\Theta}, \tag{A.9}$$

with gravity acceleration g and reference pressure $p_0 = 1000$ hPa. The mesoscale pressure deviation is given by the linearized equations

$$p' = \int_z^{z_T} g\rho' \, dz', \qquad \rho' = \bar{\rho}\left(-\frac{\Theta'}{\bar{\Theta}} - 0.608q + q_c + q_r\right), \tag{A.10}$$

with model top z_T at 15000 m.

7.2. Geostrophic forcing

The gradients in the y direction are assumed to be zero with the exception of spatially and temporarily constant terms $\partial v_g/\partial y$ and $\partial \bar{\Theta}/\partial y$ which are related to the geostrophic deformation field by the continuity equation end the thermal wind equation:

$$\frac{\partial v_g}{\partial y} = -\frac{\partial u_g}{\partial x}, \qquad \frac{\partial u_g}{\partial p} = -\gamma \frac{\partial \Theta}{\partial y},$$

$$\text{with} \quad \gamma = \frac{g}{f\Theta}. \tag{A.11}$$

These terms are very important for frontal simulation because they drive the ageostrophic circulation as described by the Sawyer Eliassen equation. The terms $u_g(\partial u_g/\partial x)$ and $v_g(\partial v_g/\partial y)$ in equations (A.5) and (A.6) represent an additional pressure term which ensures that the large scale wind field (u_g, v_g) is a solution of the model equations and therefore remains unchanged during the simulation. Strictly speaking (u_g, v_g) denotes not the geostrophic wind but a large scale gradient wind in the model equations. Nevertheless $\partial u_g/\partial x = -1.5 \cdot 10^{-5}$/s is an order of magnitude smaller than f. Thus the gradient wind is almost equal to the geostrophic wind.

7.3. *Nonhydrostatic approximation*

Substitution of the equations (A.5) and (A.7) in (A.8) leads to the Poisson equation for the pressure correction term p''

$$\nabla^2 p'' = \bar{\rho} \frac{\partial}{\partial x}\left(\frac{\partial u}{\partial t}\right)^* + \frac{\partial}{\partial z}\left(\bar{\rho}\left(\frac{\partial w}{\partial t}\right)^*\right). \tag{A.12}$$

$(\partial u/\partial t)^*$ and $(\partial w/\partial t)^*$ are the right-hand sides of equations (A.5) and (A.7) without the terms containing p''. Eq. (A.12) is solved with the conditions $w(z=0) = w(z=z_T) = 0$ at the upper and lower boundary and $p'' = 0$ at the lateral boundaries.

7.4. *Parameterization of moisture processes*

The condensation rate C of water vapor to cloud water is chosen so that q is equal to the specific humidity of saturated air q_s, as long as enough water vapor is available, with:

$$q_s = 3.78 \cdot 10^{-3} \frac{\text{kg}}{\text{kg}} \frac{p_0}{\bar{p}} \times \exp\left(\frac{L}{R_v}\left(\frac{1}{273.1K} - \frac{1}{T}\right)\right). \tag{A.13}$$

R_v is the gas constant of water vapor. The evaporation rate of rain water $-C_r$, the transition rates of cloud water to rain water by autoconversion T_a and by convalescence T_c, and the sedimentation speed of rain $-w_f$ is given by a Kessler scheme (Kessler, 1969) as described by Groß (1986):

$$-C_r = 172 \cdot 10^{-6}\,\text{m}^3\,\text{m}^{7/20}\,\text{kg}^{-13/20}\,\text{s}^{-1} \times N_0^{7/20}(q - q_s)\, q_r^{13/20}, \tag{A.14}$$

$$T_a = \max(0, 10^{-3}\,\text{s}^{-1} \times (q_c - 0.5 \cdot 10^{-3}\,\text{kg m}^{-3})), \tag{A.15}$$

$$T_c = 2935\,\text{kg}^{-7/8}\,\text{m}^{25/8}\,\text{s}^{-1} \times N_0^{1/8} q_c q_r^{7/8} \sqrt{\frac{\bar{\rho}(p_0)}{\bar{\rho}}}, \tag{A.16}$$

$$-w_f = 90.8\,\text{s kg}^{-1/8}\,\text{m}^{-9/8} \times N_0^{-1/8} q_r^{1/8} \sqrt{\frac{\bar{\rho}(p_0)}{\bar{\rho}}}, \tag{A.17}$$

with $N_0 = 10^{-7}\,\text{m}^{-4}$.

7.5. *Turbulence parameterization*

The turbulent exchange coefficient for momentum K_m is derived from the turbulent kinetic energy e_t:

$$K_m = \frac{l}{\Phi_m(\zeta)} \sqrt{0.2 e_t}$$

$$\text{with} \quad l = \frac{\kappa z}{1 + \kappa z/30\,\text{m}}, \qquad \kappa = 0.35. \tag{A.18}$$

Φ_m is the stability function from Businger (1973):

$$\begin{aligned} \Phi_m &= (1 - 15\zeta)^{-1/2} \quad \text{for} \quad \zeta \leq 0, \\ \Phi_m &= 1 + 4.7\zeta \quad \text{for} \quad \zeta > 0. \end{aligned} \tag{A.19}$$

e_t is given by a further prognostic equation:

$$\frac{\partial e_t}{\partial t} = -u \frac{\partial e_t}{\partial x} - w \frac{\partial e_t}{\partial z} + K_m \times \left(\left(\frac{\partial u}{\partial z}\right)^2 + \left(\frac{\partial v}{\partial z}\right)^2\right) - K_h \frac{g}{\bar{\Theta}} \frac{\partial \Theta_{(e)}}{\partial z} - \frac{0.08 \Phi_m(\zeta)}{l} e_t^{2/3} + \frac{\partial}{\partial x} K_h \frac{\partial e_t}{\partial x} + 1.2 \frac{\partial}{\partial z} K_h \frac{\partial e_t}{\partial z}. \tag{A.20}$$

The stability parameter ζ is derived from the local Richardson number Ri by inversion of the Businger equations:

$$\mathrm{Ri} = 0.74 \frac{(1-15\zeta)^{1/2}}{(1-9\zeta)^{1/2}} \quad \text{for} \quad \mathrm{Ri} \leqslant 0$$

and

$$\mathrm{Ri} = \zeta \frac{0.74 + 4.7\zeta}{(1+4.7\zeta)^2} \quad \text{for} \quad \mathrm{Ri} > 0, \tag{A.21}$$

with

$$\mathrm{Ri} = \frac{g}{\bar{\Theta}} \frac{\partial \Theta_{(e)}/\partial z}{(\partial \boldsymbol{v}_h/\partial z)^2 + \mu}. \tag{A.22}$$

The constant $\mu = 5 \cdot 10^{-5}\,\mathrm{s}^{-2}$ is introduced to prevent a numerical overflow when the wind shear tends to zero. In equation (A.20) and (A.22) $\partial\Theta_{(e)}/\partial z$ is equal to $\partial\Theta/\partial z$ if saturation is not reached, otherwise it is the gradient of the equivalent potential temperature:

$$\Theta_e = \Theta + \frac{L}{c_p} q_s. \tag{A.23}$$

The exchange coefficient for heat K_h is given by $K_h = K_m/\mathrm{Pr}$ with

$$\mathrm{Pr} = 0.74 \quad \text{if} \quad \zeta > 0$$

and

$$\mathrm{Pr} = 0.74 \frac{(1-15\zeta)^{1/4}}{(1-9\zeta)^{1/2}} \quad \text{if} \quad \zeta \leqslant 0. \tag{A.24}$$

7.6. *Surface fluxes*

The vertical turbulent fluxes of momentum, and sensible and latent heat at the ground (i.e., between the ground and the first grid point in 10 m height) are calculated by means of the Monin-Obukhov theory with the stability functions given by Businger (1973). The roughness length z_0 is chosen as 10^{-4} m over sea and 0.25 m over land. The temperature at z_0 is set equal to the surface temperature. The specific humidity q at z_0 is set to the saturation value q_s over sea. Over land it is parameterized as

$$q(z_0) = q(10\,\mathrm{m}) + 0.03(q_s(z_0) - q(10\,\mathrm{m})). \tag{A.25}$$

7.7. *Surface temperature*

At the surface, the balance of sensible and latent heat fluxes H_s and H_l as calculated by the Monin-Obukhov theory, the soil heat flux H, and the long-wave and short-wave radiation budgets I_l and I_s are taken into account:

$$0 = H_l + H_s + H + I_l + I_s. \tag{A.26}$$

The surface temperature changes on time scales between some minutes and 24 h, as caused by the passage of the sharp surface front and the diurnal radiation cycle, respectively. The variations of the soil heat flux H must be properly simulated over this range of time scales. Therefore it is calculated between logarithmically spaced grid points at 1, 2.7, 7.1, 18.8, and 50 cm depth there the soil temperature is calculated as a prognostic variable:

$$\frac{\partial T}{\partial t} = -\frac{1}{\rho_s c_s} \frac{\partial}{\partial z} H$$

$$\text{with} \quad H = -\nu_s \frac{\partial T}{\partial z}. \tag{A.27}$$

The soil constants density $\rho_s = 1088\,\mathrm{kg/m^3}$, heat conductivity $\nu_s = 1.05$ W/m/K and specific heat $c_s = 1700$ J/kg/K are chosen according to a sandy soil with 10% liquid water content (Pielke, 1984). Long-wave radiation budget at the surface is calculated as $I_l = \varepsilon\sigma T_s^4$, with the surface temperature T_s and the Stefan-Bolzmann constant σ. The constant $\varepsilon = 0.18$ accounts for the compensating downward radiation from the atmosphere. The short-wave radiation budget is given by $I_s = -\max(0, \mu \cos Z I_0)$, Z being the zenith angle of the sun, I_0 the short-wave radiation flux density outside the atmosphere and $\mu = 0.5$ a constant accounting for the extinction of radiation in the atmosphere and the albedo of the ground. The values of ε and μ were adapted in order to reproduce the observed development of the boundary layer height and the measured radiation budget during the field experiment on 9 May 1989 (Brümmer, 1990).

7.8. *Initialization*

The cross-front ageostrophic circulation caused by the geostrophic forcing must be considered in the initial state in order to reduce spin-up problems. The initial ageostrophic circulation is calculated diagnostically by the Sawyer Eliassen equation:

$$\frac{\partial}{\partial x}\left(\frac{\gamma}{\bar{p}}\frac{\partial\Theta}{\partial z}\frac{\partial\Psi}{\partial x}-\frac{\gamma}{\bar{p}}\frac{\partial\Theta}{\partial x}\frac{\partial\Psi}{\partial z}\right)+\frac{\partial}{\partial z}\left(\frac{1}{\bar{p}}\frac{\partial m}{\partial x}\frac{\partial\Psi}{\partial z}-\frac{1}{\bar{p}}\frac{\partial m}{\partial z}\frac{\partial\Psi}{\partial x}\right)=2fQ_1. \qquad (A.28)$$

The ageostrophic stream function Ψ is defined by $\partial\Psi/\partial z=\bar{p}(u-u_g)$ and $-\partial\Psi/\partial x=\bar{p}w$. $m=v_g+fx$ is the absolute momentum and $\gamma=g/(f\bar{\Theta})$. The Q-vector component Q_1 was defined in equation (1) in Section 2. The Sawyer Eliassen equation is solved by an iterative procedure, consistent with the discrete representation of the thermal wind equation in the model.

7.9. *Numeric solution*

The model equations are integrated explicitly with the Adams Bashford procedure with upstream differences used in the advection term. The Poisson equation is solved by a generalized conjugate gradient algorithm provided by Kapitza and Eppel (1987).

REFERENCES

Bénard, P., Redelsperger, J. P. and Lafore, J. P. 1992. Nonhydrostatic simulation of frontogenesis in a moist atmosphere. Part I: General description and narrow rainbands. *J. Atmos. Sci.* **49**, 2200–2217.

Brümmer, B. (ed.) 1990. FRONTEX 1989, Frontenexperiment im norddeutschen Küstenbereich. Bericht über die Feldmessungen mit einigen Meßbeispielen. *Hamburger Geophys. Einzelschriften* **B7**, 114.

Brümmer, B., Hennemuth, B., Rhodin, A. and Thiemann, S. 1995. Interaction of a cold front with a sea breeze front: Observations. *Tellus* **47A**, 383–402.

Dunst, M. and Rhodin, A. 1990. On the influence of frictional effects on surface fronts. *Contr. Atmosph. Phys.* **63**, 223–242.

Emanuel, K. A. 1985. What limits front formation? *Nature* **315**, 99.

Gall, R. L., Williams, R. T. and Clark, T. L. 1987. On the minimum scale of surface fronts. *J. Atmos. Sci.* **44**, 2562–2574.

Groß, G. 1986. A numerical study of the land and sea breeze including cloud formation. *Contr. Atmosph. Phys.* **59** 97–114.

Hennemuth, B., Rhodin, A. and Brümmer, B. 1992. The fog front of 25 May 1989, a gravity flow? *Meteorol. Atmos. Phys.* **48**, 273–292.

Hoskins, B. J. and Bretherton, F. P. 1971. Atmospheric frontogenesis models: mathematical formulation and solution. *J. Atmos. Sci.* **29**, 11–37.

Hoskins, B. J., Draghici, I. and Davies, H. C. 1978. A new look at the ω-equation. *Quart. J. R. Met. Soc.* **104**, 31–38.

Houze, R. A. and Hobbs, P. V. 1982. Organisation and structure of precipitating cloud systems. *Adv. in Geoph.* **24**, 225–315.

Kapitza, H. and Eppel, D. 1987. A 3-d poisson solver based on conjugate gradients compared to standard iterative methods and its performance on vector computers. *J. Comp. Phys.* **68**, 474–484.

Kessler, E. 1969. On the distribution and continuity of water substance in atmospheric circulations. *Meteorol. Monographs* **32**, 1–84.

Keyser, D. and Anthes, R. A. 1982. The influence of planetary boundary layer physics on frontal structure in the Hoskins–Bretherton horizontal shear model. *J. Atmos. Sci.* **39**, 1783–1802.

Physick, W. L. 1988. Mesoscale modeling of a cold front and its interaction with a diurnally heated land mass. *J. Atmosph. Sci.* **45**, 3169–3187.

Pielke, R. A. 1984. *Mesoscale meteorological modeling.* Academic Press, Orlando, Florida, 384.

Rhodin, A. 1991. Kaltfronten unter dem Einfluß der Reibung in der Grenzschicht und ihre Modifikation bei unterschiedlicher Bodenrauhigkeit und Bodentemperatur, Numerische Simulationen. PhD Thesis. *Ber. Zentr. für Meeres- u. Klimaforschung*, Universität Hamburg **15**, 125 pp.

Roeloffzen, J. C., Van den Berg, W. D. and Oerlemans, J. 1986. Frictional convergence at coastlines. *Tellus* **38A**, 397–411.

Shapiro, M. A., Hampel, T., Rotzoll, D. and Mosher, F. 1985. The frontal hydraulic head: a micro-α-scale ($\sim$1 km) triggering mechanism for mesoconvective weather systems. *Mon. Wea. Rev.* **113**, 1166–1183.

Simpson, J. E., Mansfeld, D. A. and Milford, J. R. 1977. Inland penetration of sea breeze fronts. *Quart. J. R. Met. Soc.* **103**, 47–76.